nature geoscience

SUPPLEMENTARY INFORMATION

DOI: 10.1038/NGEO1453

Caldera size modulated by the yield stress within a crystal-rich magma reservoir

Leif Karlstrom[1], Maxwell L. Rudolph[1], Michael Manga[1]

[1]Department of Earth and Planetary Science

University of California, Berkeley

Berkeley, CA 94720-4767

USA

Supplementary Information

Model derivation

We model an (assumed isothermal) magma chamber whose pressure P_C evolves in time due to material transfer (Figure S1) as

$$\eta \frac{dP_C}{dt} = \frac{1}{\rho_{mix}} (Q_I - Q_O) \tag{1}$$

where Q_I and Q_O are the mass fluxes of magma into and out of the chamber, ρ_{mix} is a mixture magma density and η an effective chamber volume divided by a bulk modulus[22] that accounts for deformation of the host rock as well as the three–phase mixture of bubbles, crystals and melt in the chamber. During explosive eruptions $Q_O >> Q_I$, so we consider only extraction from a fixed reservoir with fixed volume. We can treat the conduit flow as quasi-steady because the timescale for chamber pressure change

$$\tau_{chamber} \sim \frac{\Delta P_C V_C \rho_{mix}}{K_{mix} Q_O}, \tag{2}$$

is much longer than the timescale for magma ascent

$$\tau_{ascent} \sim \frac{H}{\bar{u}}, \tag{3}$$

where $\Delta P_C = P_C - \rho_s g H$ is the chamber over–pressure with g = 9.8 m/s^2, ρ_s the density of crustal rocks, H the conduit length, V_C the chamber volume and K_{mix} the effective bulk modulus.

For large eruptions we take representative values of $V_C \sim 10^{12}$ m^3, $\Delta P_C = 10^7$ Pa, conduit radius $r = 10 - 100$ m, $Q_O = \pi r^2 \bar{u} \rho_{mix}$, $K_{mix} = 10^7 - 10^9$ Pa to account for the important effect of bubbles on magma compressibility[22], $H = 7500$ m, and representative velocity $\bar{u} = 1 - 10$ m/s (below fragmentation). $\tau_{chamber} >> \tau_{ascent}$ for these parameter choices, so we assume steady conduit flow and time–dependent chamber evacuation.

Our model describes the evolution of chamber volume and pressure

$$\rho_0 V_{0,C} + \int_0^t \dot{M}(\tau) d\tau = V_C(P_C)/v_S(P_C). \tag{4}$$

Equation 4 is an equation of state for mobile fluid in the magma chamber, relating a reference (initial) undeformed chamber volume $V_{0,C}$, initial bulk density ρ_0, the deformed volume of the cavity V_C, the specific volume v_S (volume per unit mass) of the 3-phase fluid inside the chamber, the time derivative of chamber mass $\dot{M}$ and the chamber pressure P_C.

Stresses are calculated from the equations of linear elasticity

$$\nabla \cdot \underline{\sigma} = \underline{0}, \tag{5}$$

$$\sigma_{ij} = \lambda \epsilon_{kk} \delta_{ij} + 2\mu \epsilon_{ij}, \tag{6}$$

where λ and μ are the Lamé constants, subject to boundary conditions on the chamber boundary ∂S

$$\sigma_n|_{\partial S} = \Delta P_C, \tag{7}$$

and the free surface

$$\sigma_n|_{z=H} = \sigma_t|_{z=H} = 0, . \tag{8}$$

Deformed chamber volumes in equation 4 are calculated using equation 5 with possibly differing elastic moduli in the immobile portions of the chamber and the country rocks (Figure S1). σ_n and σ_t are normal and tangential stresses.

As an initial condition, we impose at and interior to the contact between locked magma and country rocks ∂R

$$\sigma_n|_{\partial R} = \Delta P_0. \tag{9}$$

This reference state accounts for the development of over–pressure $\Delta P_0 = P_0 - \rho_s g H$ in the locked magma prior to the onset of eruption. ΔP_0 should reflect the evolving rheology of crustal rocks in response to reservoir assembly. We do not address the processes of this assembly, which may occur on timescales as short as 100 years[12] to $> 10^5$ years[43]. Relaxation of elastic stresses should result in low ΔP_0, although it may theoretically vary between zero and a failure threshold. The condition that $0 \leq \Delta P_0 \leq \Delta P_C$ holds initially, but in the case of large magma yield stress $\Delta P_C \leq 0 \leq \Delta P_0$ may occur during chamber growth.

Inclusion of a reference pre–stressed state is not a feature of most magma chamber models. We believe, however, that such an initial condition accurately reflects the dichotomy in timescales (chamber construction versus evacuation) in these dynamic simulations. ΔP_0 occurs as a steady uniform pressure in the locked magma region (Figure S1) prior to mobilization. Equilibration of this pressure with that of mobilized magma does not occur because it requires pore pressure diffusion, a process that is much more slower than eruptive processes.

We model steady one–dimensional isothermal conduit flow of magma, solid particles and gas, in which conservation of mass and momentum can be expressed as[31]

$$\frac{\partial P}{\partial z} = \frac{-\left(\rho_{mix} g + f\right)}{1 - \frac{u^2}{c_s^2}}, \tag{10}$$

$$\rho_{mix} = \left(\frac{n}{\rho_g} + \frac{1-n}{\left(\frac{\chi}{\rho_s} + \frac{1-\chi}{\rho_l}\right)^{-1}} \right)^{-1} \tag{11}$$

where u is the cross–section averaged mixture velocity at height z above the magma chamber and P is pressure. Equation 11 is the density of a mixture of solid, liquid and gas with densities ρ_s, ρ_l, ρ_g, with n the mass fraction of gas (water and CO_2) calculated as a function of pressure from Papale (1999)[38] assuming Fish Canyon Tuff compositions[3]. $\chi = 0.4$ is the mass fraction of solids, taken to be constant. Although χ may vary as magma yield stress in the chamber (a parameter in our model) varies, we hold it constant for simplicity. The presence of choked flow at the vent and $\tau_{chamber} >> \tau_{ascent}$ prevent variation in all conduit flow parameters from affecting the end result of chamber evacuation, although they will affect eruptive timescales. The assumption of yielding (Bingham) rheology in the magma chamber does not conflict with equation 10, as high strain rates in the conduit ensure mobilization (at least in near wall regions of the conduit) throughout eruption. Fragmentation occurs at a critical strain rate[37], at which point the friction factor f and mixture sound speed c_s are calculated from turbulent approximations[31]. Below the fragmentation depth $c_s^2 = (\partial P/\partial \rho_{mix})$ is calculated numerically to conserve mass, while the friction factor due to laminar flow through a cylindrical pipe is

$$f = 8\Lambda \frac{\mu_m(n,\chi)u}{r^2} \tag{12}$$

with $\mu_m(n,\chi)$ the apparent viscosity. We note that f may be simply represented for other conduit geometries. Non–circular or fissure–like conduits require corrections only to this friction term. We assume that elastic stresses do not close conduits once the conduit is underpressured[29,33] because conduit erosion[23] creates pathways with small radii of curvature that remain open. In this case, available potential energy is the limiting factor for conduit flow.

$$\Lambda = \frac{1}{1 + a\left(\frac{\mathrm{Na}}{\sqrt{\mathrm{Gz}}}\right)^{1.5}} \tag{13}$$

is an empirical correction to the friction factor due to viscous heating[11] with $a = 0.3$. $\mathrm{Na} = b\mu_r \bar{u}^2/k$ is the Nahme–Griffith number measuring the relative importance of viscous heating and conduction with dimensionless $b = 0.05$; $\mathrm{Gz} = \rho_{mix} c_p \bar{u} r^2/kH$ is the Graetz number measuring vertical advective heat transport versus lateral conduction. For representative values as before and $\mu_r = \mu_m(n = 0, \chi = 0) \sim 10^7$ Pas (Fish Canyon Tuff melt composition viscosity at 750° C[3]),

Na $= 10^6 - 10^8$ and Gz $= 10^7 - 10^9$. Here c_p is specific heat capacity, and k is thermal conductivity. While likely important for silicic eruptions, the viscous heating parameterized by Λ does not significantly affect our results, which are dictated by the conduit boundary conditions (in particular choked flow).

Viscosity in our model thus depends on magma composition, water content and temperature[21], bubble[36] as well as crystal[7] volume fraction, strain rate[7], and viscous heating[11,19]. We neglect wall–localized heating and radial viscosity variation due to lateral variations in strain rate (although these are parameterized through Λ, which decreases the reference apparent viscosity by up to 3 orders of magnitude for the conditions of interest). We similarly neglect explicit treatment of temperature variations with height[32], but note that non–adiabatic temperatures and radial variation in heat transfer in the conduit during silicic super–eruptions may be reflected in textural features of erupted lavas[5] and could account for heating comparable to that attributed to magma chamber rejuvenation[3].

Equations 10-11 are subject to boundary conditions that couple time evolving chamber pressure to the conduit:

$$P|_{z=0} = \Delta P_C \tag{14}$$

and choked flow $u = c_s$ at the surface, a condition that is likely realized during most explosive eruptions[13]

$$u|_{z=H} = c_s. \tag{15}$$

We adopt a von Mises criterion for mobilizing locked magma during eruption, calculated as

$$\sigma_v = \sqrt{3J_2} \tag{16}$$

where J_2 is the second deviatoric stress invariant. If decompression induces elastic stresses in rheologically locked magma σ_v such that the von Mises yield stress σ_{magma} is exceeded, this locked magma mobilizes[40]. The result is a larger chamber radius and increased chamber pressure. Pressure increase (buffering) occurs because incorporated material has the initial pressure ΔP_0 of the locked magma. The small difference in specific volume between locked magma at the initial over–pressure and that of mobilized magma is also accounted for in this step. We assume an initial condition of no deviatoric stress within the locked, unmobilized magma at onset of eruption.

We solve for the expanding chamber radius iteratively, beginning with a spherical chamber of radius 2 km, such that von Mises stresses outside the new chamber radius are everywhere lower

than σ_{magma}. Our chamber is confined to a layer of half–thickness 2 km, so that there is one degree of freedom for chamber expansion. While this geometrical constraint is imposed for simplicity, we expect it to be approximately realized in nature, as large aspect ratio chambers and stress concentration in regions of high boundary curvature will promote lateral rather than vertical expansion. The position of the yield surface in unsteady flow of yielding fluids is a free–boundary problem with generally more structure and subtlety than our treatment. By analogy to Bingham channel flows[44] and Saffman-Taylor problems[2], we expect that boundary layers of unyielded fluid may develop during syn–eruptive mobilization of locked magma. Preferential yielding in a stratified chamber is a natural extension of this model, although it is beyond the scope of our efforts here. Magma yield stress functions only to modulate eruption time (similar to conduit flow processes) in cases where complete chamber mobilization occurs.

At each time step we evaluate maximum von Mises stress between the chamber (defined by the yield surface) and the surface, using a critical crustal yield stress σ_{cr} as a metric for failure of the crustal. This failure criterion is comparable to other possible criteria (Figure S2) such as tensional failure (set by least compressive stress σ_3) and Mohr-Coulumb shear failure (set by the difference $\sigma_1 - \sigma_3$ on planes oriented 45° from σ_1 [14]). Caldera formation models that include one or more of these criteria[14,17] are thus comparable to ours despite differences in model complexity, and qualitative results of our simulations (Figure S4) are not sensitive to the particular failure criterion. For the von Mises criterion, maximum stress magnitudes are at the surface implying initiation of failure there.

Deviatoric stresses are calculated as a departure from the reference stress distribution set by specifying the size of the locked magma reservoir and its over–pressure ΔP_0 (equation 9). Locked zone over–pressures approaching the initial mobilized chamber over–pressure represent a reference von Mises stress state that is not perturbed significantly until large under–pressures are reached. This situation progresses to caldera failure only after complete mobilization of the reservoir and chamber underpressuring. Conversely, small locked zone over–pressures allow significant von Mises stresses to accumulate during chamber growth and hence caldera formation before complete mobilization is possible.

Elastic stresses and strains (equations 5–8) are calculated numerically using the axisymmetric program mode in FEAP, version 8.3[45]. The two–point conduit boundary value problem of equation 11 is solved with a bisection and shooting method and 4th order Runge Kutta integration with

adaptive step size control. Newton–Raphson iteration is performed at each timestep to ensure the chamber pressure remains consistent both with the elastic deformation of the chamber and the withdrawal of material through the conduit.

Yielding rheology of magma

The existence and magnitude of a yield stress for crystal rich silicate melts is controversial. Although a number of experiments[7,9,25,41] and theoretical studies[24,42,46] address magma yield stress, it has been difficult to determine experimentally for the high crystal fractions and apparent viscosities of interest[9]. It is complicated by the likelihood that yield stress may vary as a function of crystal fraction and shear rate[20]. The withdrawal of crystal rich magma at eruptive rates may also push the suspension through a jamming transition[8,27], in which an effective yield stress exist at crystal volume fractions that are much lower than the maximum packing fraction. For example, flattened prismatic crystals form a percolating network at volume fractions in the range of 0.08 – 0.29[42], that may sustain elastic stresses over eruptive timescales if pushed through a jamming transition.

In the absence of predictions for yield stress that are directly applicable to silicic crystal rich magmas, we use the model of Gay et al. (1969)[15] to estimate a range of yield stresses that may be reasonable for crystal rich silicic magmas. This model is empirical, but allows us to explore yield stress as a function of parameters that can be estimated from field deposits, experiments or predicted theoretically. It also provides a comparison with the work of Burgisser and Bergantz (2011)[6], whose mechanism for chamber–wide mobilization before eruption relies on low suspension yield stress as calculated from the Gay et al. (1969) model.

Yield stress in the Gay et al. (1969) model requires estimates of the mean crystal size D_p, crystal volume fraction Φ, maximum packing fraction Φ_m, shape factor ξ and geometric standard deviation Σ. Crystal sizes in large ash–flow tuffs range considerably, from 0.1 mm – 10 mm. Mean crystal sizes are in general correlated with the crystallinity of the magmas[4], and are > 1 mm for many large eruptions. We take $D_p = 10$ mm as an upper bound from published crystal size distributions[4,34], although we experiment with sizes down to $D_p = 0.1$ mm for comparison with Burgisser and Bergantz (2011). We expect that crystal sizes as measured from erupted lavas under–represent the mean crystal size in the magma chamber as many crystals exhibit evidence of melting, fracture or breaking during eruption[19], and numerous small microlite crystals may form upon ascent[18].

Figure S3 shows yield stresses σ_{magma} as a function of crystal volume fraction Φ predicted

by this model, using shape factor $\xi = 0.5$, along with curves that represent bounds defined by $D_p = 0.1 - 10$ mm, $\Sigma = 1.25$ (a low proportion of small crystals), and $\Phi_m = 0.6 - 0.84$[6,39]. Grey boxes represent the range of Φ estimated for magma with $30 - 60\%$ crystals and $D_p = 0.5 - 10$ mm in the two cases where $\Phi_m = 0.6$ (light) and $\Phi_m = 0.84$ (dark), although we recognize that the Gay et al. model may not be valid as Φ approaches Φ_m[39]. $\Phi_m = 0.6$ is the classical maximum packing for geological fluids[28], while 0.84 exceeds the hexagonal close packing of mono–dispersed spheres (0.74) but is used to compare with Burgisser and Bergantz (2011)[6]. Predicted yield stress for this range of crystallinity lies in the range of $\sigma_{magma} = 10^1 - 10^7$ Pa. Figure S3 highlights that magma yield stress is poorly constrained. We use a wide range of values to reflect this uncertainty, with the difference between pressures $\Delta P_C - \Delta P_0$ providing a reference value that is consistent with initial conditions for triggering eruption (Table S1).

Clearly better characterization of yield stress is required to constrain this aspect of our model. We note that yield stress is a quantity defined before flow occurs, i.e., the stress required to initiate motion. Once yielding occurs, magma deforms viscously. Small yield stresses measured in lavas after mobilization (e.g., Pinkerton and Stevenson, 1992[39]) thus do not characterize the quantity of interest in our model and are lower bounds to magma yield stress.

Parameter space

We perform 3000 Monte Carlo simulations sampling the parameter space in Table 1 to explore the dynamics of our model, and to generate data that may be compared to caldera forming eruptions in the geologic record. Field constraints include total discharge and caldera size, while estimates exist for other parameters of dynamical importance: magma volatile content, chamber crystallinity (yield stress), magma viscosity, chamber depth, the caldera scale strength of roof rocks (the critical von Mises stress σ_{cr}), conduit radius, and difference in elastic moduli (Young's Modulus $E_{cr} - E_{magma}$ and Poisson's Ratio $\nu_{cr} - \nu_{magma}$) between locked magma and country rocks, lateral extent (aspect ratio) of locked magma reservoir. Some of these parameters are better constrained than others.

We fix the volume of the crystal rich reservoir to be a disk with rounded edges of half–thickness 2 km, situated at 7.5 km depth (Figure S1). This depth is similar to estimates for magma emplacement pressures (2–3 kbar[26]). We vary the lateral radius of stored magma between 5 and 30 km, which corresponds to roof aspect ratios (depth/diameter) of 0.75–0.125. Aspect ratio may exert primary control on the final geometry of collapse calderas[1,29], however studies to date do not consider

the mechanical consequences of only partially fluid reservoirs during collapse. We assume a fixed CO_2 mass fraction of $n_{CO2} = 0.1$, but a uniform prior distribution of all other parameters (Table 1).

Figure S4 shows that caldera forming eruptive volumes are bimodal, with different parameter dependence for the case of complete mobilization (blue symbols) versus partial mobilization (red symbols) at caldera collapse. Volumes comparable to super–eruptions (> 500 km^3) require full mobilization and depend in a meaningful way only on the strength of country rocks – the critical roof rock von Mises stress σ_{cr} – and locked zone radius (roof aspect ratio). The yield stress of magma is constrained from below by the pressure difference between locked magma and initial mobile chamber, and the combination of these three parameters determine whether complete mobilization can occur (see also main text Figure 2.c). Contrast in elastic parameters between locked magma and country rocks does not appear to affect erupted volumes, although we note that different choices of country rock Young's modulus affects the magnitude of strain in crustal rocks in response to chamber pressure changes and hence the likelihood of caldera failure. For our chosen $E_{crust} = 10$ GPa, we find a small subset of results ($\sim 1\%$) in which strains become large and unphysical displacements occur in finite element simulations. Linear elasticity breaks down as strains approach order unity, so we discard simulations in which this occurs. Figure S4.f shows that conduit radius does not affect the results, given choked flow at the surface. Variation in magma volatile content and Poisson's ratio contrast between crustal rocks and locked magma (not plotted) similarly do not affect the results.

Volcanic eruption data

We use data from two sources to compare our model results with real eruptions. For Holocene eruptions, we use the Smithsonian Institution Global Volcanism Program database. This database has been demonstrated to be complete through eruption of magnitude 4 and larger[10]. Eruption magnitude is defined generally as a combination of data from plume height and volume erupted[30,35]. We use a formula based solely on erupted volume

$$\mathrm{M} = \log_{10}(DRE) - 7 \tag{17}$$

where DRE is the Dense Rock Equivalent magma mass in kilograms to calculate eruption magnitude for all our data.

For caldera forming eruptions, we use the worldwide Collapse Caldera Database (CCDB)[16] to estimate magnitude and frequency of volcanic eruptions that are most similar to those we model.

This database includes calderas that vary in age from historical eruptions up to 500 Ma, although the age distribution peaks around 30 Ma[16]. We expect that there are systematic preservation biases reflected in this wide age distribution. We use the upper limits reported for eruption volume in DRE.

We model silicic, crystal rich caldera forming eruptions that begin with a phase of eruptive activity that precedes caldera collapse. We thus filter the CCDB to study the statistics of such eruptions in the geologic record. The total number of eruptions with volume estimates in the database is 137. We divide these into two compositional categories, "mafic" and "felsic," including as felsic anything with an evolved composition including dacite and rhyolite eruptions, as well as more exotic compositions such as trachyte. Basalt and andesite eruptions are considered mafic, as are phonolites and latites. Felsic eruptions in the CCDB number 115, and preserve the multi-modal distribution of eruption volumes seen in the full dataset (Figure S6).

Further filtering would ideally be done to best match our model. Unfortunately, the number of eruptions in the CCDB that contain simultaneous data on volume, composition and pre–caldera activity drops considerably. As Figure S6 indicates, *n* drops to 39 when considering these three fields. We find that two–thirds or more of CCDB eruptions exhibit a pre–caldera eruptive sequence. Due to preservation biases this is a lower bound.

We finally add crystallinity (using maximum reported numeric value) as a field with which to filter the CCDB. With four fields to match the number of available data points drops to 13, as crystallinity data in the CCDB are sparse. Of this small dataset we find that no eruption with volume greater than 100 km^3 records a crystal content less than 26%, and only 2 eruptions are reported with no pre-caldera activity. Maximum reported crystallinity is 75%. Further development of the CCDB and the sources for this data will no doubt allow for more thorough exploration of relevant eruptions.

An additional test of our model predictions is offered by CCDB data on caldera diameter. As Figure S7.a shows, maximum caldera diameter does not appear to be a reliable predictor of eruption volume as diameter decreases (for example, both a 20 km and 85 km diameter caldera produced ~ 1000 km^3 magma). This is consistent with our inference that reservoir size does not necessarily control caldera diameter. And although statistics are sparse, the increased crystallinity of eruptions at low maximum caldera diameter (Figure S7.b) is consistent with our prediction that high yield stress magmas are more prone to caldera formation at small radius and partial mobilization.

Given the sparsity of highly filtered subsets of the CCDB, we use a subset containing felsic

eruptions only to construct the distribution of caldera forming eruptions in Figure 3. Quantitative comparison of this and the Holocene data to Monte Carlo simulations was carried out using a Kolmogorov–Smirnov (KS) test with a significance level of 5%. Based on this test, both simulated and database derived caldera forming eruptions arise from a different underlying distribution than the complete Holocene eruption catalog at 95% confidence. The complete distribution of caldera forming eruptions and model results also fail this similarity test, however if we exclude caldera forming eruptions smaller than 3 km^3 from both datasets the two distributions pass the KS test indicating that the model results best align with data from larger eruptions. We expect that refining the prior distribution of input parameters would permit a better match to observational data, as would including smaller locked magma zones (the lower size limit considered here is 5 km radius).

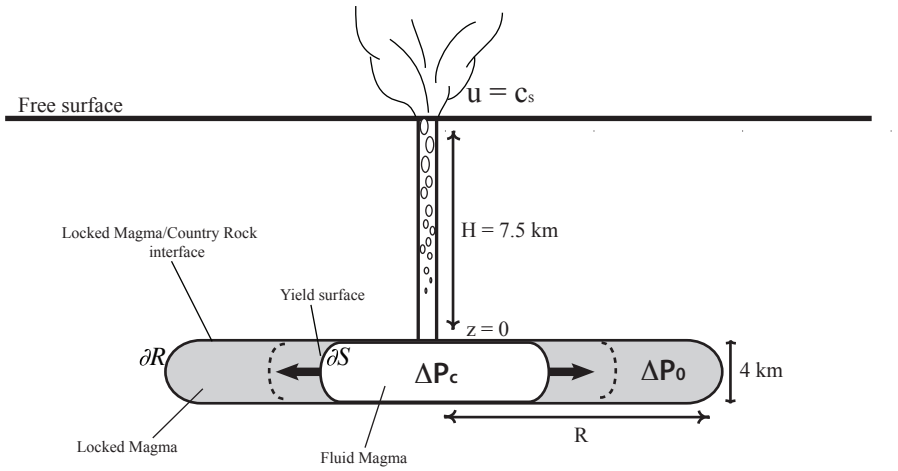

Figure 1: Model geometry and boundary conditions, illustrating the three material regions that enter into the magma chamber equation of state. Conduit length is fixed, while lateral extent of crystal rich magma R is variable. Note that the pressure ΔP_0 applied between boundaries ∂R and ∂S is an initial condition.

References

[1] V. Acocella. Understanding caldera structure and development: An overview of analogue models compared to natural calderas. *Earth-Science Reviews*, 85:125–160, 2007.

[2] A. N. Alexandrou and V. Entov. On the steady-state advancement of fingers and bubbles in a Hele-Shaw cell filled by a non-Newtonian fluid. *European Journal of Applied Mathematics*, 8:73–87, 1997.

[3] O. Bachmann, M. Dungan, and P. Lipman. The Fish Canyon magma body, San Juan Volcanic Field, Colorado: rejuvenation and eruption of an upper-crustal batholith. *Journal of Petrology*, 43(8):1469–1503, 2002.

[4] I. N. Bindeman. Crystal sizes in evolving silicic magma chambers. *Geology*, 31(4):367–370,

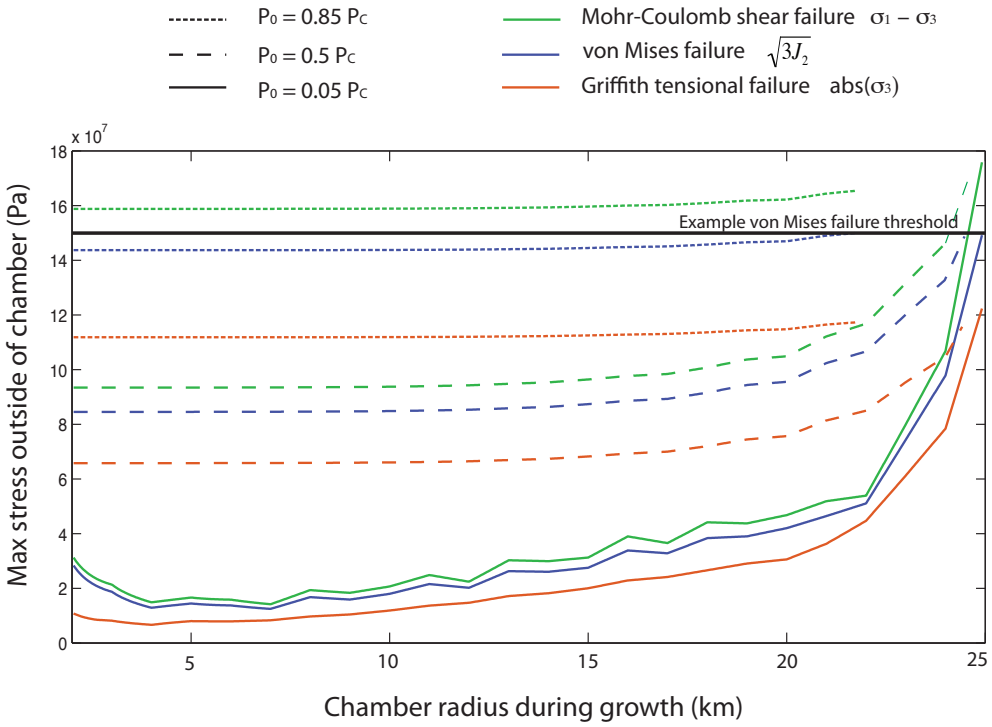

Figure 2: Comparison of maximum von Mises stress magnitude $\sqrt{3J_2}$ in the domain to other possible failure criteria, for an example simulation of caldera failure prior to complete mobilization. In this example $\sigma_{crit} - \sigma_{magma}$ = 50 MPa, ΔP_C = 10 MPa, all other parameters as in Figure 2. Tensional failure is modeled by least principle deviatoric stress σ_3 (red curves) while Mohr-Coulumb shear failure on planes 45° from the σ_1 (maximum principle devatoric stress) direction is described by $\sigma_1 - \sigma_3$. Note that as ΔP_0 increases maximum stresses become dominated by that of the press-stressed initial condition, and that von Mises failure occurs at smaller chamber radius.

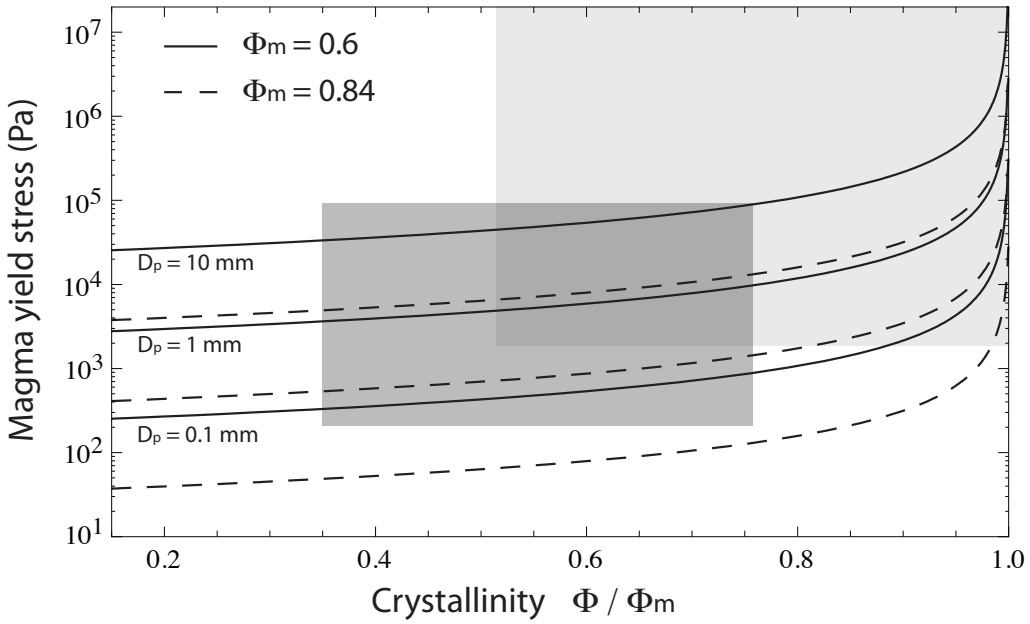

Figure 3: Yield stress as a function of crystallinity (normalized by the maximum packing fraction) predicted by the semi–empirical model of Gay et al. (1969)[15]. Parameters used are described in the text. Boxes represent a range of crystal rich magmas ($30-60\%$) with light grey assuming maximum packing $\Phi_m = 0.6$ and dark grey $\Phi_m = 0.84$.

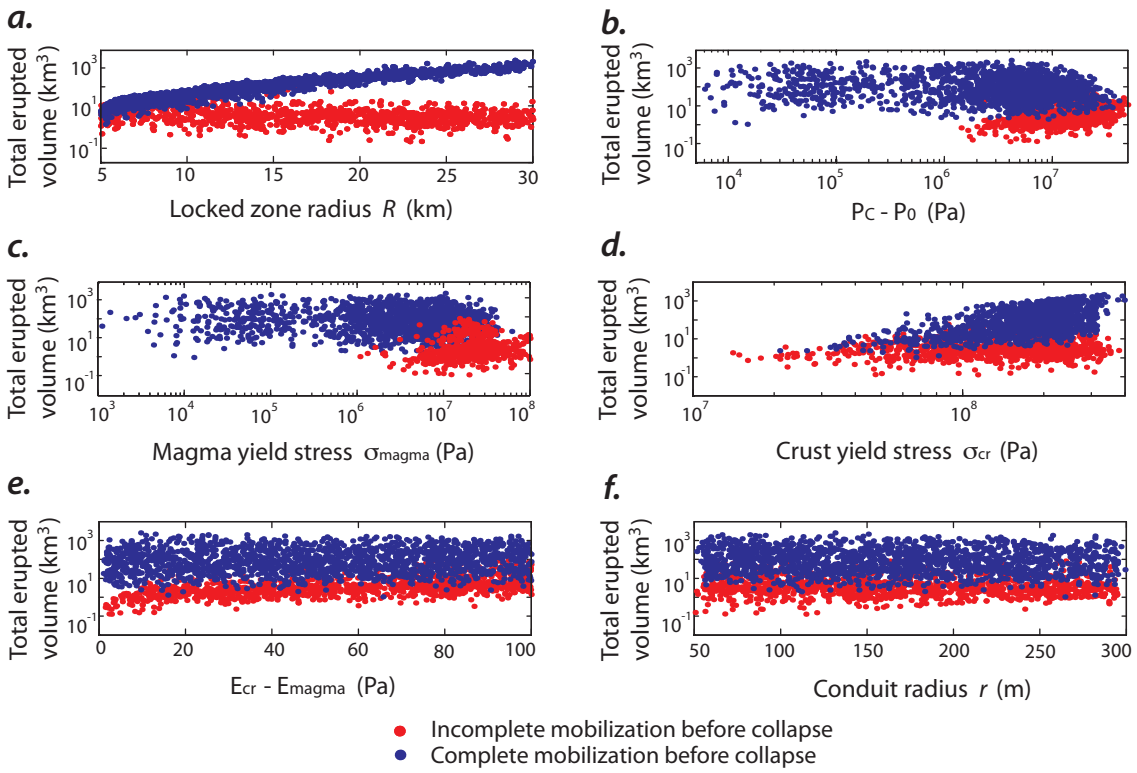

Figure 4: Monte Carlo results, plotting final discharge in km^3 as a function of **a**, Locked zone radius (initial reservoir dimension) **b**, Difference between initial triggering over–pressure in mobile magma and initial locked magma pressure. **c**, Magma yield stress **d**, Crust yield stress **e**, Young's modulus difference between country rocks and locked magma **f**, Conduit radius. Completely mobilized chambers (blue symbols) have different dependencies than incompletely mobilized chambers (red symbols).

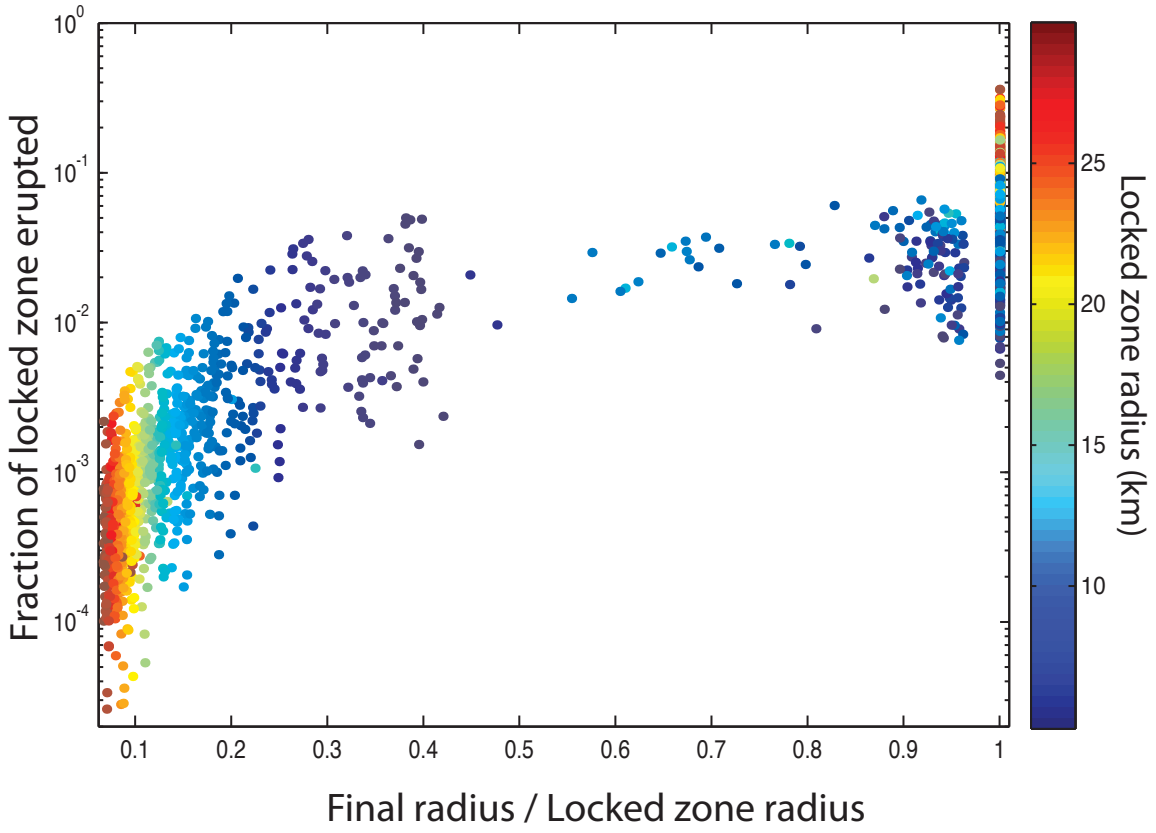

Figure 5: Fraction of locked zone erupted as a function of fractional radius mobilized at onset of caldera collapse. A significant fraction of calderas form with radius less than 50% the locked zone radius. For these there is a straightforward correlation with fraction of reservoir erupted. Only for completely mobilized chambers does the fraction erupted exceed 10% of the reservoir.

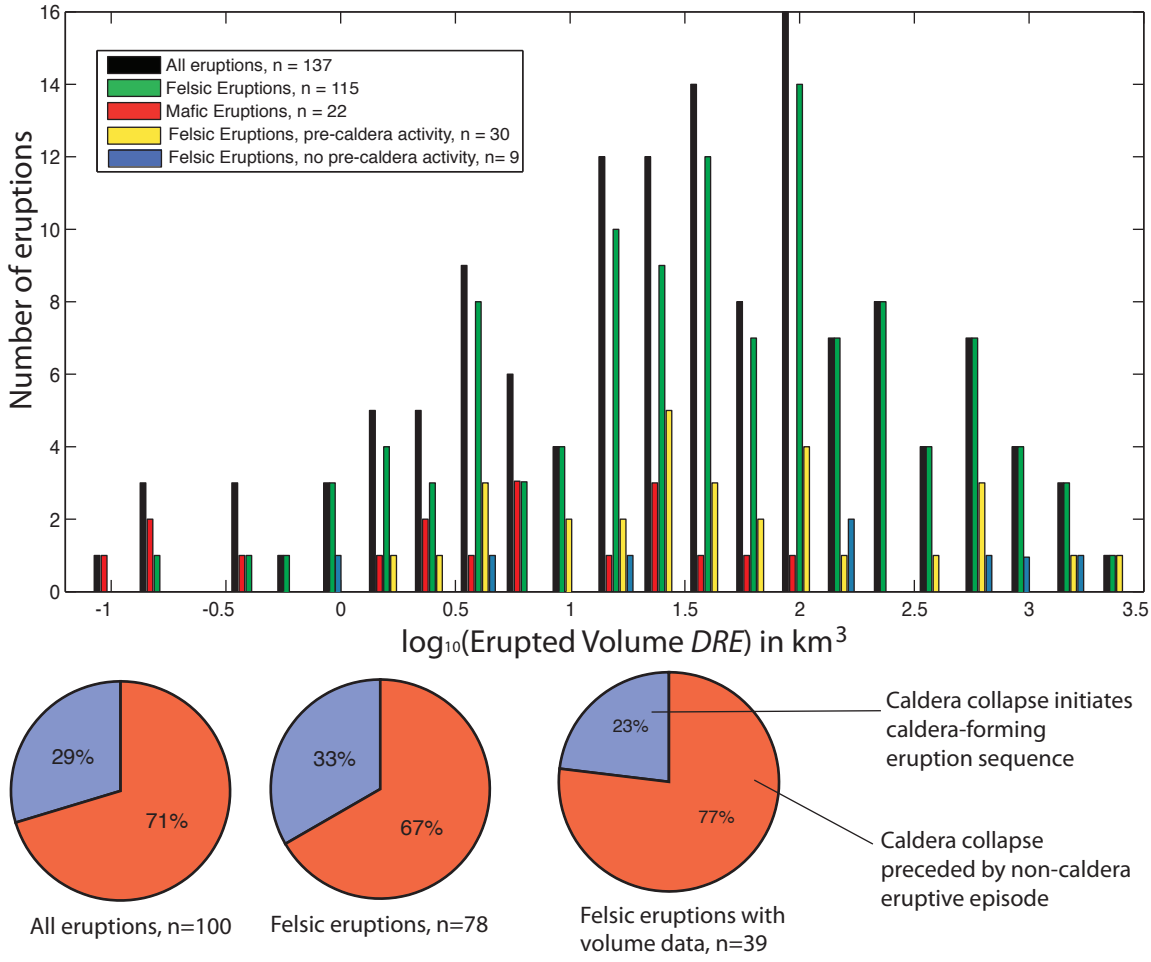

Figure 6: Filtering of the Collapse Caldera Database. Histogram illustrates the distribution of observed eruption sizes as increasing restrictions are placed on data. Pie charts show relative proportion of eruptions exhibiting pre-caldera eruption deposits, for various filter choices. Discussion of filter criteria provided in the text.

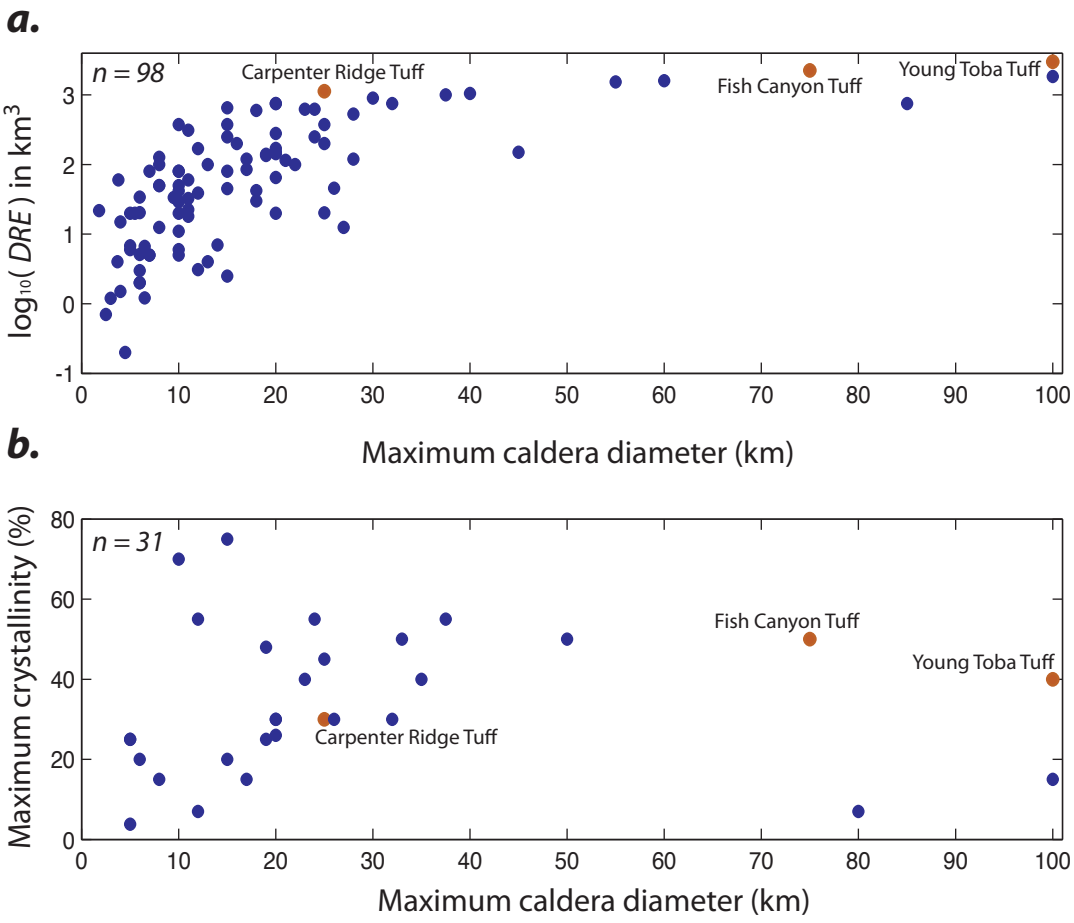

Figure 7: a. Relationship between maximum caldera diameter and eruption volume (in dense rock equivalent, DRE) from the Collapse Caldera database. b. Crystallinity as a function of caldera diameter. Labeled eruptive deposits are highlighted in each panel.

Monte Carlo parameters

Parameter Name	Symbol	Range [Min ; Max]
Locked zone radius	R	$[5\,;30]$ km
Initial mobile magma over–pressure	ΔP_C	$[5\,;50]$ MPa
Locked zone over–pressure	ΔP_0	$[0\,;\Delta P_C]$
Magma yield stress	σ_{magma}	$[(P_C - P_0)/4\,;4(P_C - P_0)]$
Country rock yield stress	σ_{cr}	$[\sigma_{magma}\,;10^{8.5}]$ Pa
Conduit radius	r	$[50\,;300]$ m
Country rock Young's modulus	E_{cr}	10^{10} Pa
Magma Young's modulus	E_{magma}	$[10^8\,;10^{10}]$ Pa
Country rock Poisson ratio	ν_{cr}	0.25
Magma Poisson ratio	ν_{magma}	$[0.25\,;0.4]$
Magma water content	$\mathrm{n} - \mathrm{n}_{CO2}$	$[3\,;7]$ weight percent

Table 1: Range of model parameters in Monte Carlo simulations. Uniform distributions are assumed.

2003.

[5] J. Blundy, K. Cashman, and M. Humphreys. Magma heating by decompression-driven crystallization beneath andesite volcanoes. *Nature*, 443:76–80, 2006.

[6] A. Burgisser and G. W. Bergantz. A rapid mechanism to remobilize and homogenize highly crystalline magma bodies. *Nature*, 471(7337):212–215, 2011.

[7] L. Caricchi, L. Builini, P. Ulmer, T. Gerya, M. Vassalli, and P. Papale. Non-newtonian rheology of crystal-bearing magmas and implications for magma ascent dynamics. *Earth and Planetary Science Letters*, 264:402–419, 2007.

[8] M. E. Cates, J. P. Wittmer, J.-P. Bouchaud, and P. Claudin. Jamming, force chains, and fragile matter. *Physical Review Letters*, 81(9):1841–1844, 1998.

[9] R. Champallier, M. Bystricky, and L. Arbaret. Experimental investigation of magma rheology at 300 MPa: From pure hydrous melt to 76 vol. % of crystals. *Earth and Planetary Science Letters*, 267:571–583, 2008aa.

[10] S. Coles and R. Sparks. Extreme value methods for modeling historical series of large volcanic magnitudes. In H. Mader, S. Coles, C. Connor, and L. Connor, editors, *Statistics in volcanology*, volume 1 of *Special Publication of IAVCEI*, pages 47–56. London: Geologocal Society, 2006.

[11] A. Costa, O. Melnik, and E. Vedeneeva. Thermal effects during magma ascent in conduits. *Journal of Geophysical Research*, 112(B12205), 2007.

[12] T. Druitt, F. Costa, E. Deloule, M. Dungan, and B. Scaillet. Decadal to monthly timescales of magma transfer and reservoir growth at a caldera volcano. *Nature*, 482:77–80, 2012.

[13] J. Dufek and G. W. Bergantz. Transient two-dimensional dynamics in the upper conduit of a rhyolitic eruption: A comparison of closure models for the granular stress. *Journal of Volcanology and Geothermal Research*, 143:113–132, 2005.

[14] A. Folch and J. Marti. Geometrical and mechanical constraints on the formation of ring-fault calderas. *Earth and Planetary Science Letters*, 221:215–225, 2004.

[15] E. C. Gay, P. A. Nelson, and W. P. Armstrong. Flow properties of suspensions with high solids concentration. *AlChE Journal*, 15(6):815–822, 1969.

[16] A. Geyer and J. Marti. The new worldwide collapse caldera database (CCDB): A tool for studying and understanding caldera processes. *Journal of Volcanology and Geothermal Research*, 175(3):334–354, 2008.

[17] A. Gudmundsson. Effect of tensile stress concentration around magma chambers on intrusion and extrusion frequencies. *Journal of Volcanology and Geothermal Research*, 35:179–194, 1988.

[18] J. Hammer, K. Cashman, R. Hoblitt, and S. Newman. Degassing and microlite crystallization during pre-climactic events of the 1991 eruption of Mt. Pinatubo, Philippines. *Bulletin of Volcanology*, 60(5):355–380, 1999.

[19] K.-U. Hess, B. Cordonnier, Y. Lavallée, and D. B. Dingwell. Viscous heating in rhyolite: An in situ experimental determination. *Earth and Planetary Science Letters*, 275:121–126, 2008.

[20] L. Heymann, S. Peukert, and N. Aksel. On the solid-liquid transition of concentrated suspension in transient shear flow. *Rheologica Acta*, 41:307–315, 2002.

[21] H. Hui and Y. Zhang. Toward a general viscosity equation for natural anhydrous and hydrous silicate melts. *Geochimica et Cosmochimica Acta*, 71:403–416, 2007.

[22] H. Huppert and A. Woods. The role of volatiles in magma chamber dynamics. *Nature*, 420 (6915):493–495, 2002.

[23] B. Kennedy, O. Spieler, B. Scheu, U. Kueppers, J. Taddeucci, and D. Dingwell. Conduit implosion during vulcanian eruptions. *Geology*, 33(7):581–584, 2005.

[24] R. C. Kerr and J. R. Lister. The effects of shape on crystal settling and on the rheology of magmas. *The Journal of Geology*, 99(3):457–467, 1991.

[25] A.-M. Lejeune and P. Richet. Rheology of crystal-bearing silicate melts: An experimental study at high viscosities. *Journal of Geophysical Research*, 100(B3):4215–4229, 1995.

[26] P. Lipman. Incremental assembly and prolonged consolidation of Cordilleran magma chambers: Evidence from the Southern Rocky Mountain Volcanic Field. *Geosphere*, 3(1):42–70, 2007.

[27] A. J. Liu and S. R. Nagel. Jamming is not just cool any more. *Nature*, 396:21–22, 1998.

[28] B. D. Marsh. On the crystallinity, probability of occurrence, and rheology of lava and magma. *Contributions to Mineralogy and Petrology*, 78:85–98, 1981.

[29] J. Marti, A. Geyer, A. Folch, and J. Gottsmann. A review on collapse caldera modeling. In J. Gottsmann and J. Marti, editors, *Developments in Volcanology*, volume 10, chapter 6, pages 233–283. Elsevier, 2008.

[30] B. G. Mason, D. Pyle, and C. Oppenheimer. The size and frequency of the largest explosive eruptions on earth. *Bulletin of Volcanology*, 66:735–748, 2004.

[31] L. G. Mastin. Insights into volcanic conduit flow from an open-source numerical model. *Geochemistry Geophysics Geosystems*, 3(7), 2002.

[32] L. G. Mastin and M. S. Ghiorso. Adiabatic temperature changes of magma-gas mixtures during ascent and eruption. *Contributions to Mineralogy and Petrology*, 141:307–321, 2001.

[33] P. McLeod. The role of magma buoyancy in caldera-forming eruptions. *Geophysical Research Letters*, 26(15):2299–2302, 1999.

[34] A. Mock and D. A. Jerram. Crystal size distributions (CSD) in three dimensions: Insights from the 3D reconstruction of a highly porphyritic rhyolite. *Journal of Petrology*, pages 1–17, 2005.

[35] C. G. Newhall and S. Self. The volcanic explosivity index (VEI): An estimate of explosive magnitude for historical volcanism. *Journal of Geophysical Research*, 87(C2):1231–1238, 1982.

[36] R. Pal. Rheological behavior of bubble-bearing magmas. *Earth and Planetary Science Letters*, 207:165–179, 2003.

[37] P. Papale. Strain-induced magma fragmentation in explosive eruptions. *Nature*, 397:425–428, 1999.

[38] P. Papale. Modeling of the solubility of a two-component H_2O + CO_2 fluid in silicate liquids. *American Mineralogist*, 84:477–492, 1999.

[39] H. Pinkerton and R. J. Stevenson. Methods of determining the rheological properties of magmas at sub-liquidus temperatures. *Journal of Volcanology and Geothermal Research*, 53: 47–66, 1992.

[40] M. Rudolph, L. Karlstrom, and M. Manga. A prediction of the longevity of the Lusi mud eruption, Indonesia. *Earth and Planetary Science Letters*, 308(124-130), 2011.

[41] F. J. Ryerson, H. C. Weed, and A. J. Piwinskii. Rheology of subliquidus magmas 1. Picritic compositions. *Journal of Geophysical Research*, 93(B4):3421–3436, 1988.

[42] M. O. Saar, M. Manga, K. V. Cashman, and S. Fremouw. Numerical models of the onset of yield strength in crystal-melt suspensions. *Earth and Planetary Science Letters*, 187:367–379, 2001.

[43] U. Schaltegger, P. Brack, M. Ovtcharova, I. Peytcheva, B. Schoene, A. Stracke, M. Marocchi, and G. Bargossi. Zircon and titanite recording 1.5 million years of magma accretion, crystallization and initial cooling in a composite pluton (southern Adamello batholith, Northern Italy). *Earth and Planetary Science Letters*, 286:208–218, 2009.

[44] A. J. Taylor and S. D. Wilson. Conduit flow of an incompressible, yield-stress fluid. *Journal of Rheology*, 41(1):93–101, 1997.

[45] R. L. Taylor. Feap: A finite element analysis program. *User Manual*, 2008.

[46] S. D. C. Walsh and M. O. Saar. Numerical models of stiffness and yield stress growth in crystal-melt suspensions. *Earth and Planetary Science Letters*, 267:32–44, 2008.